Hindawi
Advances in Astronomy
Volume 2023, Article ID 5525558, 11 pages
https://doi.org/10.1155/2023/5525558

Research Article

Numerical Simulation and Test Study on Track Welding of QTT

Duoxiang Xu,[1,2] **Qian Xu**,[1,3,4] **Lin Li**,[1,5] **Hui Wang**,[1,3,4] **and Na Wang**[1,3,4]

[1]*Xinjiang Astronomical Observatory, Chinese Academy of Sciences, Urumqi 830011, China*
[2]*University of Chinese Academy of Sciences, Beijing 100049, China*
[3]*Key Laboratory of Radio Astronomy, Chinese Academy of Sciences, Urumqi 830011, China*
[4]*Key Laboratory of Xinjiang Radio Astrophysics, Urumqi 830011, China*
[5]*School of Physics and Technology, Xinjiang University, Urumqi 830046, China*

Correspondence should be addressed to Qian Xu; xuqian@xao.ac.cn

Received 2 December 2022; Revised 26 February 2023; Accepted 9 March 2023; Published 23 March 2023

Academic Editor: Fernando Aguado Agelet

Considering the stringent requirement of the pointing accuracy up to 2.5″ of the world's largest full steerable radio telescope, this paper studies the welding experiment of the azimuth track of the antenna. First, the opposite deformation jig and welding process were designed for the QTT's azimuth track. Then, the welding process was numerically simulated using a finite element model. The simulation results show that a better welding effect will be obtained by appropriately reducing the opposite force on the basis of the original. The three deformation processes of the track are regulated by the opposite deformation jig. The results show that the opposite deformation jig designed for QTT's azimuth track can make the amount of deformation and flatness meet the design requirements. Finally, nondestructive testing was carried out to check the welding quality of the track surface and interior. The results show that there are no obvious defects in the welds of the azimuth track. The constraint jig and welding processes designed for QTT are effective and feasible.

1. Introduction

The world's largest fully steerable radio telescope (Qitai Radio Telescope, QTT), which will be built in Qitai County, Xinjiang, China, has a diameter of 110 m, an observation frequency band of 150 MHz to 115 GHz, an overall antenna weight of about 6000 t, and a pointing accuracy of 2.5 arc seconds (arcsec) [1, 2]. This places extremely high demands on the load-bearing properties of the azimuth track [3]. In the actual construction of a high-precision, large aperture antenna azimuth track using integral welding technology instead of the common splicing track technology for small and medium-diameter antennas [4, 5]. However, the sectional welding technique requires filling the weld groove with a large amount of welding material, and this method will cause welding distortion. Therefore, it is necessary to analyze and study the deformation and weld quality of azimuth track. This will reduce the influence of the azimuth track on the pointing accuracy and even the stability of the antenna.

There are some classical solutions at home and abroad in the welding design of the azimuth track of large radio telescopes. The Mexico 50 m Radio Telescope (LMT) uses a narrow-band clearance groove welding process [6, 7]. Each of the two sections of the track is fixed to the base plate by fillet welding, and a suitable amount of opposite deformation is given by bending the base plate so that the flatness of the entire track is within 0.3 mm after the welding is finished. The 100 m radio telescope (GBT) in the USA uses the same welding process as the LMT for its composite track [8–10]. After welding, the flatness of the entire track was controlled to within 0.127 mm. The Italian 64 m Radio Telescope (SRT) uses a symmetrical welding process [11]. This type of welding requires two people to perform the top and back welding simultaneously, which can better offset the thermal deformation of the welding. However, this welding process has high requirements for overhead position welding technology. In China, the Shanghai 65 m Radio Telescope uses the narrow-clearance groove section welding method to complete the welding of the whole track [12, 13]. In this

method, the entire track is manufactured in 30 sections, of which 15 segments are welded together at the construction site. The final flatness of the track reaches 0.5 mm. The above several classic track welding schemes provide a good reference for the track welding of QTT. In addition, it is necessary to perform a finite element simulation of the QTT track welding process prior to welding to avoid costly waste.

Using numerical simulation to analyze the welding process of large structural parts, the advantages of finite element simulation in calculating the hardening properties of elastoplastic materials can be effectively used [14–16]. In practical engineering applications, welding deformation will often accompany the welding process [17, 18]. Uncontrollable-welding deformation will also lead to complex straightening processes and expensive subsequent machining costs. Based on this, many scholars use professional welding simulation software to improve the quality and performance of welded components and optimize the welding process [19, 20]. Yang reviewed recent advances in mitigation techniques that have been applied in the structural design, manufacturing, and postweld stages and analyzed the residual stress relief method of each stage [21, 22]. Ma et al. conducted a quantitative study on the effect of jig constraints on welding deformation. The effects of the jig on longitudinal shrinkage, transverse shrinkage, and angular deformation were discussed in detail [23]. Napitupulu et al. simulated welding joints and compared the simulation results [24]. Yi et al. simulated the welding process of the stiffened plate structure of a large container ship using the finite element analysis method, and the test validated the applicability of the simulation results to its prediction [25]. Akbari and Asadi used the thermo-mechanically coupled three-dimensional finite element method model to numerically simulate the FSP process and studied the material flow and particle distribution in the base metal and improved the properties of the A356 cast alloy [26].

Based on the abovementioned analysis, it can be seen that the combination of finite element simulation and welding experiments has been widely used. However, as the diameter of the QTT's azimuth track reaches 76 m, the width of each track is 630 mm, the thickness is 240 mm, and the overall flatness of the track is required to be 0.3 mm (peak to peak value) [2]. Such high precision requirements pose a significant challenge for track to be welded in the field. At present, there are no welding experiments and welding data related to it. Therefore, obtaining welding data for the azimuth track is crucial for the construction of QTT. In the preconstruction phase of the QTT, this study designed an opposite deformation jig for the QTT's azimuthal track and carried out welding experiments for the QTT's azimuthal track. Combined with the results of finite element analysis, the welding deformation of the QTT's azimuthal track was accurately measured. Through the designed opposite deformation jig, the welding deformation of the QTT's azimuth track is controlled within the design range. This provides data to support the field welding of the QTT's azimuth track at a later stage.

2. Modeling and Simulation

According to the characteristics of the azimuth track welding process, the following assumptions are made:

(1) The initial temperature of the track is the preheating temperature.

(2) The heat source moves at a constant rate, and the temperature in the center of the molten pool is uniform load.

(3) The convection and radiation effects between the track and the environment will be loaded in the form of heat flux density.

(4) Factors such as chemical reactions, stirring, convection, and radiation inside the molten pool are not taken into account.

2.1. Governing Equation and Boundary Conditions. The heat input and heat transfer processes during the welding of the azimuth track have a great influence on both the solid-state phase transition and the microstructure properties. This process is a typical nonstationary heat transfer process, and its control equation is [27]

$$\frac{\partial}{\partial x}\left(\lambda(T)\frac{\partial T}{\partial x}\right)+\frac{\partial}{\partial y}\left(\lambda(T)\frac{\partial T}{\partial y}\right)+\frac{\partial}{\partial z}\left(\lambda(T)\frac{\partial T}{\partial z}\right)=C_p(T)\rho(T)\frac{\partial T}{\partial t}. \tag{1}$$

There are three types of boundary conditions for the welding temperature field:

(1) The temperature values on the boundary are specified as follows:

$$\begin{aligned}\tau &= 0, T(0,x,y,z),\\ &= T_0(x,y,z).\end{aligned} \tag{2}$$

(2) The heat flux density values on the boundary are specified as follows:

$$-\lambda(T)\frac{\partial T}{\partial n}|\tau = 0. \tag{3}$$

(3) The surface heat transfer coefficient between the object on the boundary and the surrounding fluid and the temperature of the surrounding fluid are specified as follows [27, 28]:

$$-\lambda(T)\frac{\partial T}{\partial n}|\tau = h(T_W - T_F). \tag{4}$$

In equations (1)–(4), λ (T) is the material thermal conductivity $(\mathrm{W}\cdot(\mathrm{m}\cdot{}^\circ\mathrm{C})^{-1})$; C_p (T), the specific heat $(\mathrm{kJ}\cdot(\mathrm{kg}\cdot{}^\circ\mathrm{C})^{-1})$; ρ (T), the density $(\mathrm{kg}\cdot\mathrm{m}^{-3})$; τ, the time(s); h, the heat convection coefficients $(\mathrm{W}\cdot(\mathrm{m}^2\cdot{}^\circ\mathrm{C})^{-1})$; T_W, the ambient temperature (°C); T_F, the peripheral temperature (°C). In this study, the first type of boundary condition is loaded onto the two side surfaces of the track. The second type of boundary condition is loaded onto the upper surface of the track.

2.2. Heat Source Models. The choice of heat source model has a crucial influence on welding. The double ellipsoidal heat source takes into account the distribution of heat flow density in the thickness direction and the simulation results have the characteristics of large melting depths [29, 30]. Therefore, the double ellipsoidal heat source is suitable for the numerical simulation of thick plate welding process [31]. The double ellipsoidal heat source model was chosen for the numerical simulations in this study. The intermediate temperature in the simulations was set to 280°C.

The expression for the heat flux density distribution in the front half of the heat source model is as follows:

$$Q_{\mathrm{f}}(x, y, z) = \frac{6\sqrt{3} f_{\mathrm{f}} q_0}{abc_f \pi \sqrt{\pi}} \exp\left(-\frac{3x^2}{{c_f}^2} - \frac{3y^2}{a^2} - \frac{3z^2}{b^2}\right). \quad (5)$$

The expression for the heat flux density distribution in the rear half of the heat source model is as follows:

$$Q_{\mathrm{r}}(x, y, z) = \frac{6\sqrt{3} f_{\mathrm{r}} q_0}{abc_r \pi \sqrt{\pi}} \exp\left(-\frac{3x^2}{{c_r}^2} - \frac{3y^2}{a^2} - \frac{3z^2}{b^2}\right). \quad (6)$$

In equations (5) and (6), Q (x, y, z) is heat density at a point (x, y, z) $(\mathrm{J/mm^3})$; a, b, c_f, and c_r are geometric parameters that define the size and shape of the ellipses and, consequently, the distribution of the heat source; f_f and f_r are fractions of the heat flux imposed in the front and rear quadrants, respectively. The relationship between the two parameters is shown in equation (7). q_0 is the effective energy input of the heat source, which can be obtained by equation (8).where η is the thermal efficiency; U is the welding voltage and I is the welding current.

$$f_f = \frac{2c_f}{c_f + c_r}, f_f = \frac{2c_f}{c_f + c_r}, \quad (7)$$

$$q_0 = \eta U I. \quad (8)$$

In this study, the values of parameters in the other literature were referenced [18, 32, 33]. $a = 6$ mm, $b = 3$ mm, $c_f = 6$ mm, $c_r = 12$ mm, $\eta = 0.75$, $U = 25$ V, $I = 190$ A.

2.3. Meshing. In order to more realistically simulate the force state of the azimuth track, the constraint force and the opposite force are applied separately in the 3D model, as shown in Figure 1. The overall dimensions of the two tracks are $2600 \times 630 \times 240$ mm. The cross-section of the track to be welded is U-shaped. The cross-section has an upper width of 55 mm, a lower width of 26 mm, and a depth of 90 mm. The height of the boss, where the track is in contact with the antenna roller, is 10 mm.

Given the large number of meshes and computational efficiency, it is necessary to adjust the density of the meshes. In areas near the welds, a fine mesh is used to improve the accuracy of the calculation. In areas farther from the welds, a coarse mesh is used to improve computational efficiency, as shown in Figure 2.

The number of adjusted meshes is about 109,500, accounting for 91.6% of the fine meshes in the welds area. The number of layers and passes of the weld is set by the heat source trajectory. To reduce the amount of calculation and improve the calculation efficiency, the weld is set to 11 layers and 37 passes.

The force state of the track model is set in the simulation software, as shown in Figure 3. The forces on the track model include gravity, support, constraint, and opposite forces. The constraint force acts vertically downward on the surface of the track, and the opposite force acts vertically upward on the stressed plate at the bottom of the track. The stressed plate can evenly distribute the opposite force near the welds.

In simulations where no opposite force is applied, welding deformation occurs in the heat-affected zone of the track. Therefore, in this welding simulation, the local opposite force is added to cause the welding heat-affected zone of the track to produce opposite deformation before welding. This amount of opposite deformation is the same as the amount of welding deformation without applying opposite force, which counteracts the deformation caused by the welding process.

3. Experiment Procedures

An opposite deformation jig was designed for the welding of the QTT's azimuth track, and welding tests on the track were carried out. The test process can be divided into three stages: opposite deformation before welding, preheating and welding, and measurement after welding.

3.1. Opposite Deformation. The azimuth track of the antenna to be welded is hoisted onto the opposite deformation jig, and a downward constraint force is applied to the track. The flatness of the track is controlled to within 0.01 mm by continuously adjusting the size of the constraint force at 12 positions. The process requires real-time measurements using a laser theodolite. After leveling the azimuth track, an upward opposite force is applied to the stress plate to cause upward opposite deformation near the welds, as shown in Figure 4.

3.2. Preheating and Welding. The preheating temperature is related to factors such as the size of the base material, the chemical composition, the shape of the zone to be welded, and the hydrogen content of the filler metal. The calculation formula is as follows:

$$T_0 = 550 \bullet (c - 0.12) + 0.48h, \quad (9)$$

where T_0 is the preheating temperature (°C); c is the carbon content of the base material (%); h is the thickness of the base material (mm).

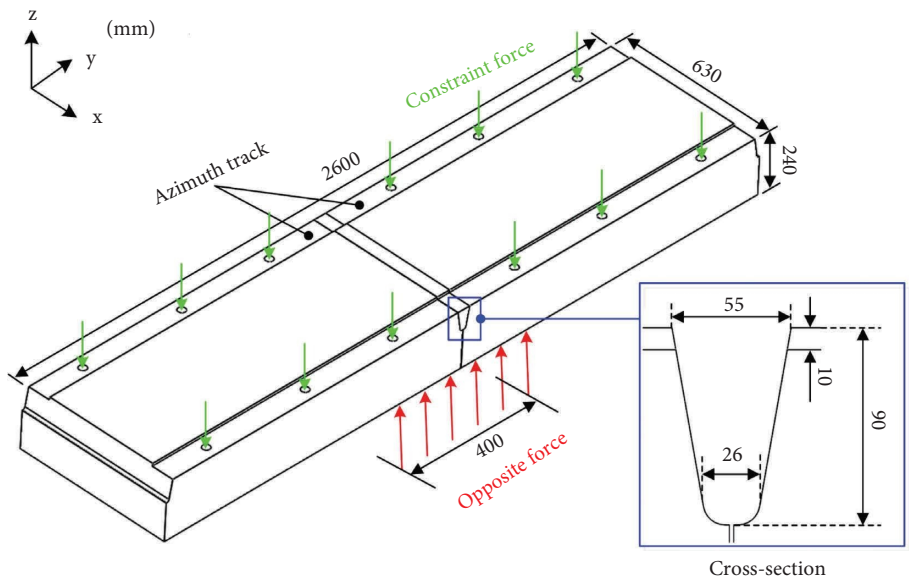

Figure 1: The 3D model of the antenna's azimuth track.

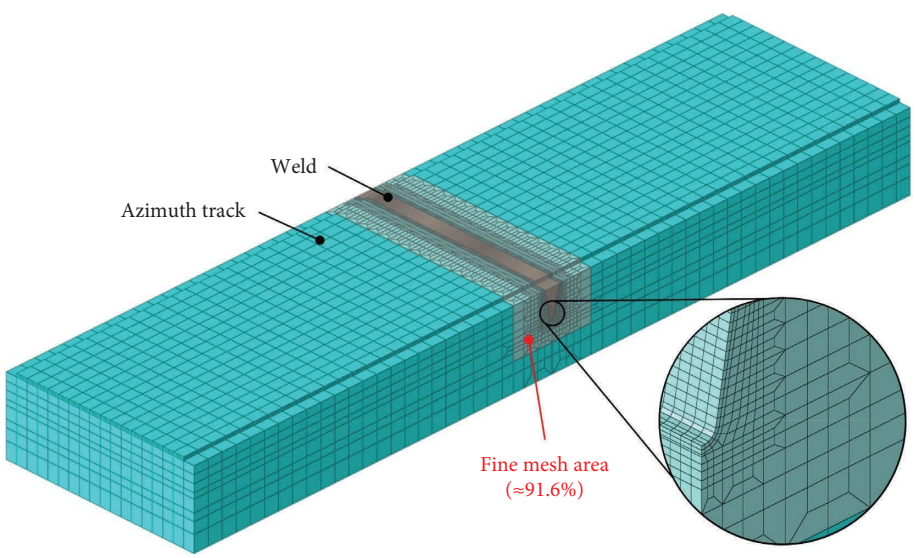

Figure 2: Meshing of the antenna's azimuth track.

The filler material used in this experiment is J607Ni (AWS: E9015-G). The weld base material is 42CrMo(ASTM: 4140). The chemical composition and mechanical properties of the two materials are shown in Tables 1 and 2, respectively. Based on the thickness of the track in Figure 1 and the carbon content of 42CrMo in Table 1, T_0 is calculated to be 281°C.

The welding process and parameters can have a significant impact on the quality of the welds. Referring to the relevant literature [34], choose the welding method as SMAW, set the welding voltage to 25 V, welding current to 190 A and welding speed to 20 cm/min. Heat the area to be welded to 280°C and hold for 3 hours, then start welding, as shown in Figure 5.

In Figure 5, the red part in (a) is the heating and insulation area around the welds. (b) collect the temperature of the welding area with an infrared thermal imager. (c) manual welding of azimuth track, the whole process lasts about 14 h. The surface of the weld is continuously struck with a pneumatic hammer during welding to remove the coating and release the stress.

4. Results and Discussion

4.1. Numerical Study. The total deformation cloud and the residual stress cloud of the azimuth track are obtained by numerical simulation, as shown in Figures 6 and 7, respectively. The y axis represents the track length and the z axis represents the track height.

As can be seen in Figure 6, the total deformation near the welds after the simulation is completed is the largest, about

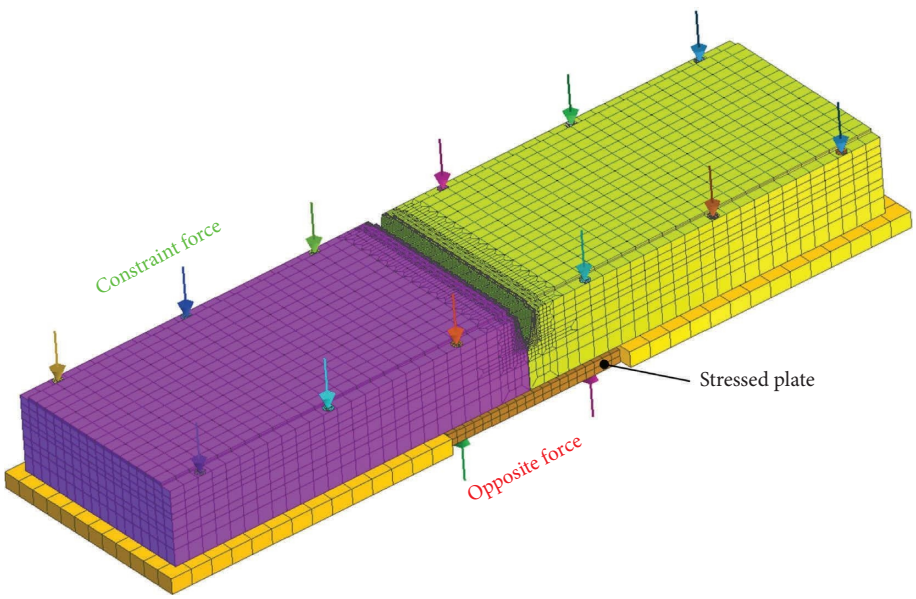

Figure 3: The state of force on the antenna's azimuth track.

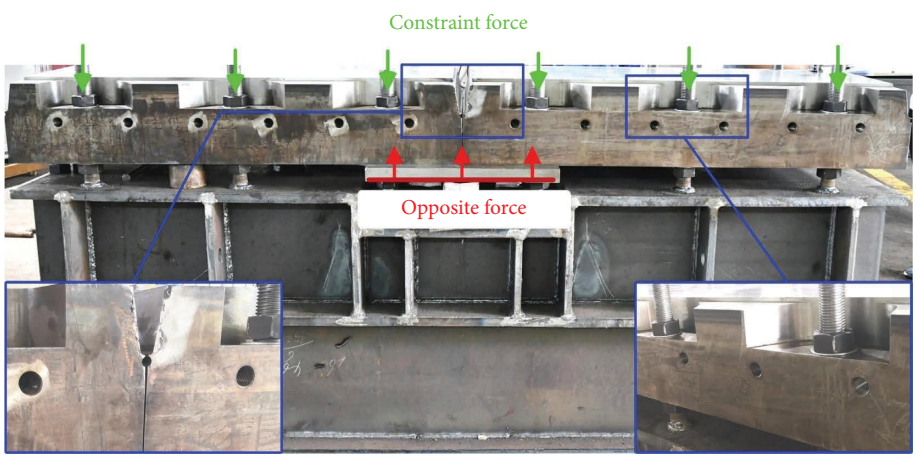

Figure 4: Leveling and opposite deformation of the antenna's azimuth track.

Table 1: Chemical composition of 42CrMo(4140) and J607Ni(E9015-G).

Wt.%	C	Cr	Mn	Si	Mo	S	P	Ni
42CrMo	0.42	1.05	0.65	0.27	0.20	≤0.035	≤0.035	≤0.03
J607Ni	≤0.12	0.25	1.00	≤0.80	0.20	≤0.030	≤0.030	1.35

Table 2: Mechanical properties of 42CrMo(4140) and J607Ni(E9015-G).

Material	Ultimate tensile strength (MPa)	Yield strength (MPa)	Elongation (%)
42CrMo	≥1080	≥930	≥12
J607Ni	≥590	≥490	≥15

0.33 mm. The deformation far from the welds is very small under the combined influence of its own gravity, supporting force, and constraint force, all within 0.1 mm.

Due to the constraint force and the opposite force near the welds, the deformation originally generated during the welding process is effectively suppressed by the opposite

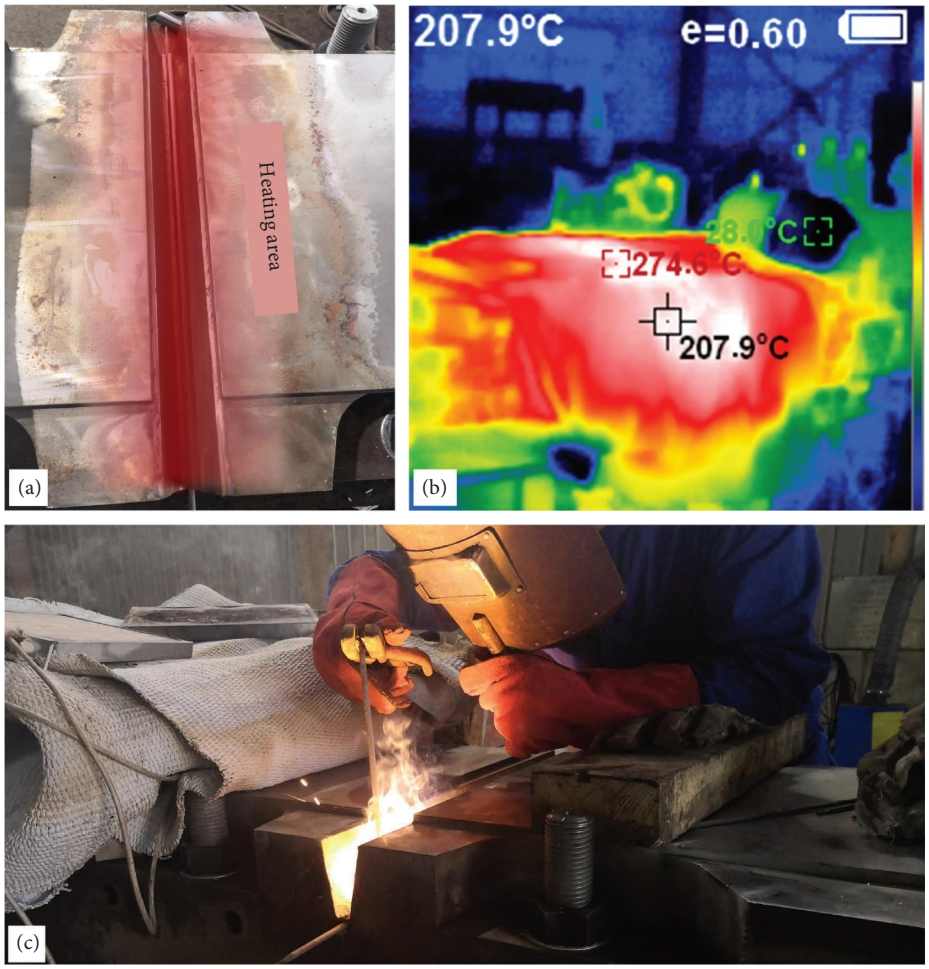

Figure 5: Preheating and welding of the antenna's azimuth track. (a) Heated and insulated welding area. (b) Acquisition of temperature data for welding. (c) Welding process of the antenna's azimuth track.

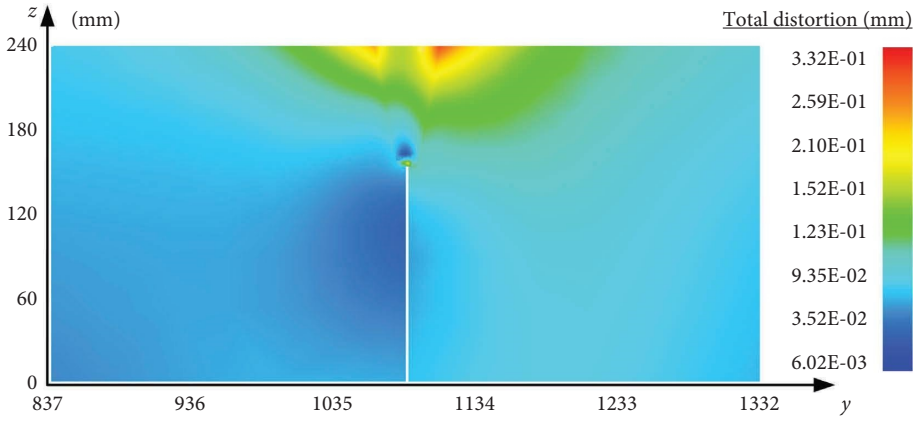

Figure 6: Total deformation of the antenna's azimuth track.

deformation generated by the opposite force. However, the simulation results show that the maximum deformation of the azimuth track exceeds the design requirement by 0.3 mm. This may be caused by excessive opposite force being applied to the track. Therefore, in welding experiments, the opposite force needs to be reduced to reduce the amount of opposite deformation of the track.

Figure 7 shows the residual stresses of the track model after simulation. It can be seen that after the cooling is

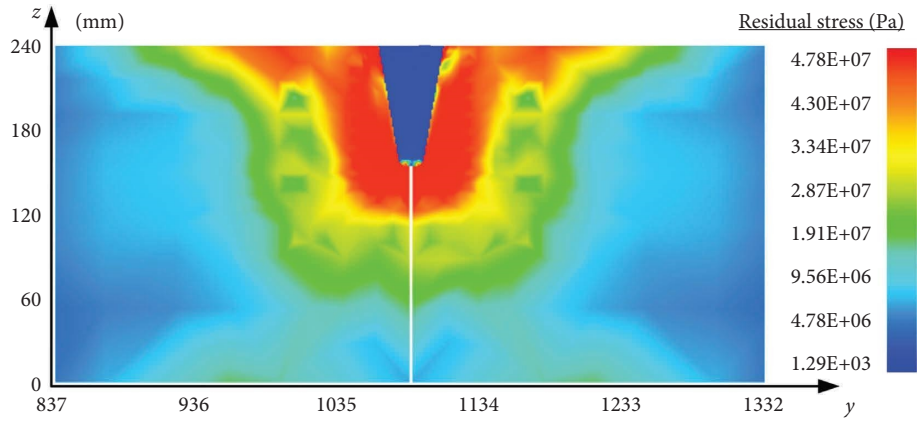

Figure 7: Residual stress of the antenna's azimuth track.

complete, the residual stress near the welds is 47.8 MPa and the residual stress away from the welds is gradually decreasing.

The trend of residual stresses perpendicular to the welds' direction has been shown to be strongly related to the constraint conditions [35]. Residual stress can be effectively reduced by heat treatment and surface treatment methods [36], such as tempering treatment, which can reduce residual stresses by 65% [37]. Therefore, in welding experiments, heat treatments such as tempering and holding are adopted for the welded track.

4.2. Nondestructive Testing (NDT). After welding, the welds are inspected on-site for NDT. Magnetic particle testing [38] and ultrasonic testing [39] are widely used for inspection of welds quality due to their respective advantages. Therefore, we choose magnetic particle testing and ultrasonic testing to inspect the quality of the polished track, as shown in Figure 8.

Figure 8(a) shows the grinding of the uppermost welds of the azimuth track. In multilayer, multipass welding of azimuth track, the latter weld has a heat treatment effect on the previous weld. This is equivalent to normalizing the previous weld and improving the secondary crystallization of the previous weld [40]. Therefore, after welding is completed, weld a layer on the track surface to improve the quality of the welds. (b) shows the magnetic particle testing of the weld on the azimuth track. The results show that there are multiple path lines on the surface of the track. These path lines are not necessarily welding cracks, they may be caused by poor manual grinding precision or a mesh residual of austenite [41]. (c) shows the ultrasonic testing of the welds on the azimuth track. The presence of clutter in the instrument indicates the presence of microcracks within the welds of the track. However, the position of the microcrack is at a depth of 40 cm~50 cm in the track, which is basically not affected by the antenna load, so it will not have a substantial impact on the life of the azimuth track.

4.3. Measurement of Flatness. During the welding process of the azimuth track, the height values at 12 positions on the track surface are measured several times using a laser theodolite. The results of multiple measurements are compared as shown in Figure 9. *A* represents the measured value before welding; *B* represents the measured value after welding; *C* represents the measured value after manual adjustment after welding.

The azimuth track was deformed three times during the welding process, which included the opposite deformation caused by the jig (before *A*), the deformation caused by welding (from *A* to *B*), and the deformation caused by manual adjustment (from *B* to *C*).

The deformation process from *A* to *B* shows that the relative height of the track near the welds is significantly reduced after welding. The deformation decreases from 2.25 to 0.375 mm and the flatness decreases from 2.25 to 0.375 mm. This indicates that the opposite deformation jig and the opposite deformation before welding offset some of the deformation during the welding process.

Even if the welding deformation of the track is effectively controlled, it is still very difficult to completely eliminate it. To make the flatness of the track meet the design requirements, it is also necessary to manually adjust the flatness of the track again by using the opposite deformation jig. The deformation process from *B* to *C* shows that the deformation of the azimuth track is reduced from 0.375 to 0.175 mm after manual adjustment. The flatness of the manually adjusted track was 0.225 mm measured with a laser theodolite. The result met the design requirements.

4.4. Measurement of Side Clearance. During the welding of the azimuth track, the side clearance of the track was measured several times. This clearance is located below the welds and the stress relief hole. Figure 10(a) indicates the size of the side clearance before applying the opposite force and (b) indicates the size of the side clearance after applying the opposite force. The measurement results show that the side

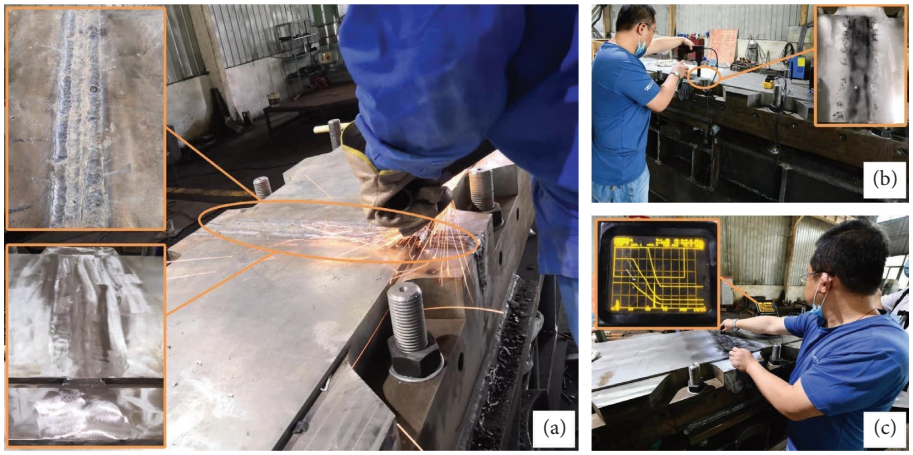

Figure 8: Weld inspection of the antenna's azimuth track. (a) Grinding of the track. (b) Magnetic particle testing of the weld. (c) Ultrasonic testing of the weld.

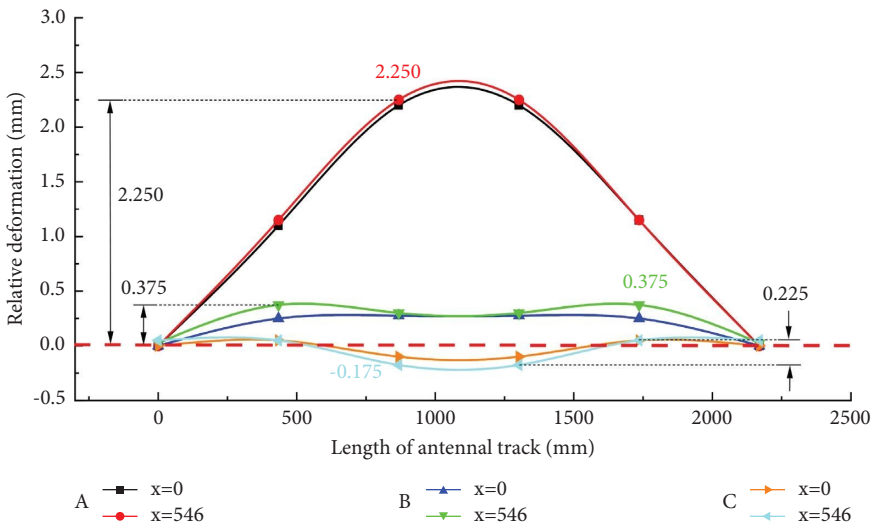

Figure 9: Deformation and flatness of the antenna's azimuth track.

clearance was about 2.5 mm before the opposite force was applied. After applying the opposite force, the upper part of the side clearance expanded to 2.97 mm and the lower part reduced to 2.04 mm.

Combined with the simulation results and related studies [36, 37], the track was maintained at 280°C for 3 hours to reduce residual stress after welding was complete. When the temperature of the track returns to room temperature, the side clearance is measured, and the results are shown in Figure 11. (a) indicates the size of the side clearance before welding and (b) indicates the size of the side clearance after welding.

Comparing Figures 10(b) and 11(a), it can be seen that the side clearance of the azimuth track changes before and after heating. Due to the thermal expansion during the heating process, the side clearance of the track shrinks by 1 mm. Since the track is heated evenly, the degree of shrinkage is also relatively uniform.

From Figures 11(a) and 11(b), it can be seen that the upper part of the side clearance is reduced by 1.39 mm and the lower part is reduced by 0.45 mm. We analyze that the phenomenon is caused by a combination of thermal expansion of the azimuth track and welding deformation during the welding process. Although side clearance of the azimuth track is not used as an evaluation indicator of welding quality, recording the variation value of the side clearance throughout the welding process will provide experience for welding on-site the QTT's azimuth track.

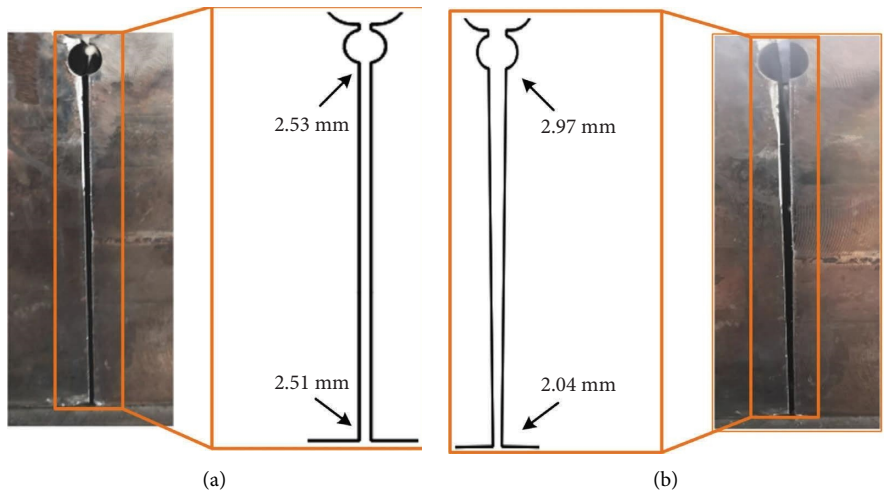

Figure 10: Comparison of the side clearance of the azimuth track. (a) Side clearance before the opposite force is applied. (b) Side clearance after the opposite force is applied.

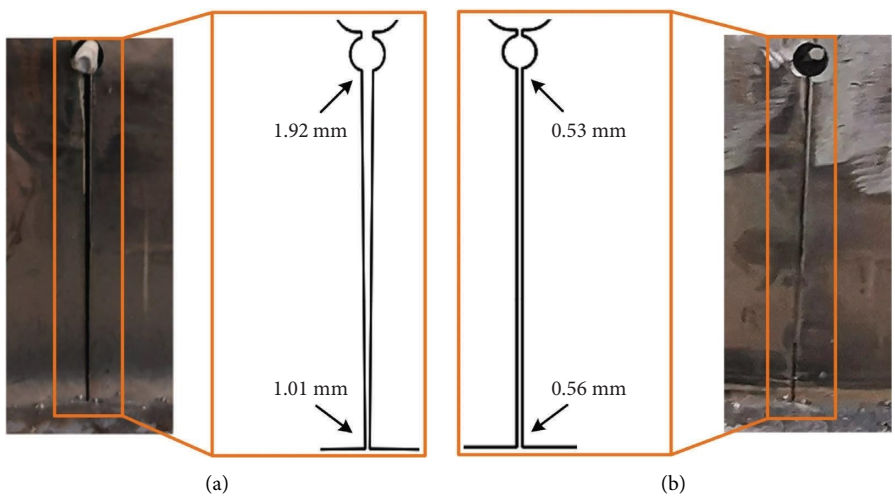

Figure 11: Comparison of the side clearance of the azimuth track. (a) Side clearance before welding. (b) Side clearance after welding.

5. Conclusions

In order to obtain the experimental data of welding applicable for QTT's azimuth track, and study and improve the feasibility of welding process applicable for QTT's azimuth track, experiments were performed. After welding, the welds of the track with 42CrMo as the base material were inspected by magnetic particle testing and ultrasonic testing. The flatness of the track was measured with a theodolite. In addition, an opposite deformation jig was designed for the QTT's track. The welding process of the track under the constraint of the opposite deformation jig was simulated using the finite element method. The conclusions can be summarized as below.

After the opposite deformation process constrained by the jig and the deformation process of welding, the clearance located under the stress relief hole of the track shrinks by about 2 mm.

There are three deformations of the azimuth track that occurred during the welding process. The opposite deformation jig designed for the QTT reduces the welding deformation of the track by 1.4 mm. Finally, the flatness of the two tracks was reduced from 2.2 mm to 0.3 mm.

The numerical simulation shows that the opposite deformation generated by the opposite deformation jig offsets the welding deformation of the track to 0.33 mm, and the residual stress after welding is 47.8 MPa. The heat treatment

after welding and appropriate reduction of the opposite force applied to the track will obtain better welding results.

NDT shows that although there are microcracks at a depth of 40 cm~50 cm in the track, this position does not bear the main load of the antenna, so it does not affect the life of the azimuth track.

The track used in this experiment is the same as the QTT's azimuth track, which will provide experience and data to support the construction of the QTT.

Data Availability

Some standard data for the metallic materials used in this study were obtained from the ASTM publicly accessible website (https://www.astm.org/products-services/bos.html). Other data that support the findings of this study are available from the corresponding author (xuqian@xao.ac.cn) upon reasonable request.

Conflicts of Interest

The authors declare that they have no conflicts of interest.

Acknowledgments

This work was supported by the National Key Research and Development Program of China (No. 2021YFC2203601), the Youth Innovation Promotion Association, CAS (No. Y202019), Natural Science Foundation of Xinjiang Autonomous (No. 2022D01E85), and the Operation, Maintenance, and Upgrading Fund for Astronomical Telescopes and Facility Instruments, budgeted from the Ministry of Finance of China (MOF) and administrated by the Chinese Academy of Sciences (CAS).

References

[1] N. Wang, "Xinjiang Qitai 110 m radio telescope," *Scientia Sinica*, vol. 44, no. 8, p. 783, 2014.

[2] N. Li, B. Duan, X. Li, B. Zheng, and J. Wu, "A reverse-design strategy for the track error of the qi tai telescope based on pointing accuracy," *Engineering*, vol. 13, pp. 209–216, 2022.

[3] P. Lian, C. Wang, S. Xue et al., "Future research trend for improving large reflector antenna service performance," *Engineering*, vol. 7, no. 8, pp. 1047–1050, 2021.

[4] H. J. Kaercher, "Azimuth axis design for huge telescopes: an update," *Astronomical Structures and Mechanisms Technology*, vol. 5495, pp. 67–76, 2004.

[5] L. Olmi and G. Grueff, "SRT: design and technical specifications," *Memorie della Società Astronomica Italiana Supplement*, vol. 10, p. 19, 2006.

[6] J. Antebi and F. W. Kan, "Precision continuous high-strength azimuth track for large telescopes," *Future Giant Telescopes*, vol. 4840, pp. 612–623, 2003.

[7] D. R. Smith, "Achievable alignment accuracy and surface hardness of a large welded azimuth track," *Optomechanical Technologies for Astronomy*, vol. 6273, pp. 322–330, 2006.

[8] A. Symmes, R. Anderson, and D. Egan, "Improving the Service Life of the 100-meter green Bank Telescope Azimuth track," *Ground-based and Airborne Telescopes II*, vol. 7012, pp. 1225–1236, 2008.

[9] N. Li, J. Wu, B. Y. Duan, and C. S. Wang, "Effect of the rail unevenness on the pointing accuracy of large radio telescope," *Acta Astronautica*, vol. 132, pp. 13–18, 2017.

[10] E. White, F. D. Ghigo, R. M. Prestage et al., "Green Bank Telescope: o," *Astronomy & Astrophysics*, vol. 659, p. A113, 2022.

[11] G. Tofani, G. Alvito, R. Ambrosini, and B. Pietro, "Status of the sardinia radio telescope project," *Ground-based and Airborne Telescopes II*, vol. 7012, pp. 162–173, 2008.

[12] B. Du, Y. Zheng, Y. Zhang, Z. Shen, and Q. Fan, "Progress in SHAO 65m radio telescope antenna," in *Proceedings of the International Symposium On Antennas & Propagation*, vol. 1, pp. 14–16, Nanjing, China, October 2013.

[13] L. Fu, J. Wang, Y. Jiang et al., "Improvement of the pointing precision of the Tianma radio telescope with an inclinometer measurement system," *Experimental Astronomy*, vol. 48, no. 1, pp. 49–64, 2019.

[14] M. Knoerr, J. Lee, and T. Altan, "Application of the 2D finite element method to simulation of various forming processes," *Journal of Materials Processing Technology*, vol. 33, no. 1-2, pp. 31–55, 1992.

[15] A. Moarrefzadeh, S. Shahrooi, and M. J. Azizpour, "The application of the meshless local Petrov-Galerkin method for the analysis of heat conduction and residual stress due to welding," *International Journal of Advanced Manufacturing Technology*, vol. 104, no. 1-4, pp. 723–742, 2019.

[16] X. Peng, G. Xu, A. Zhou, Y. Yang, and Z. Ma, "An adaptive Bernstein-Bézier finite element method for heat transfer analysis in welding," *Advances in Engineering Software*, vol. 148, Article ID 102855, 2020.

[17] W. Liang, D. Deng, S. Sone, and H. Murakawa, "Prediction of welding distortion by elastic finite element analysis using inherent deformation estimated through inverse analysis," *Welding in the World*, vol. 49, no. 11-12, pp. 30–39, 2005.

[18] H. M. Aarbogh, M. Hamide, H. Fjær, A. Mo, and M. Bellet, "Experimental validation of finite element codes for welding deformations," *Journal of Materials Processing Technology*, vol. 210, no. 13, pp. 1681–1689, 2010.

[19] M. Slováček, V. Diviš, L. Junek, and V. Ochodek, "Numerical simulation of the welding process — distortion and residual stress prediction, heat source model determination," *Welding in the World*, vol. 49, no. 11-12, pp. 15–29, 2005.

[20] Y. Mikami, T. Kawabata, T. Tagawa et al., "Numerical simulation of residual stress modification by reverse bending of notched fracture toughness test specimens of multipass welds," *Theoretical and Applied Fracture Mechanics*, vol. 92, pp. 214–222, 2017.

[21] Y. P. Yang, "Recent advances in the prediction of weld residual stress and distortion - Part 1," *Welding Journal*, vol. 100, no. 5, pp. 151–170, 2021.

[22] Y. P. Yang, "Recent advances in the prediction of weld residual stress and distortion - Part 2," *Welding Journal*, vol. 100, no. 6, pp. 193–205, 2021.

[23] N. Ma, H. Huang, and H. Murakawa, "Effect of jig constraint position and pitch on welding deformation," *Journal of Materials Processing Technology*, vol. 221, pp. 154–162, 2015.

[24] R. A. M. Napitupulu, C. Hutabarat, C. S. P. Manurung, Y. H. Manurung, and M. Graf, "Comparative study between MSC marc/mentat student version and simufact welding for three-passed butt joint," *IOP Conference Series: Materials Science and Engineering*, vol. 852, no. 1, Article ID 012071, 2020.

[25] M. S. Yi, D. H. Lee, H. H. Lee, and J. K. Paik, "Direct measurements and numerical predictions of welding-induced

initial deformations in a full-scale steel stiffened plate structure," *Thin-Walled Structures*, vol. 153, Article ID 106786, 2020.

[26] M. Akbari and P. Asadi, "Simulation and experimental investigation of multi-walled carbon nanotubes/aluminum composite fabrication using friction stir processing," *Proceedings of the Institution of Mechanical Engineers - Part E: Journal of Process Mechanical Engineering*, vol. 235, no. 6, pp. 2165–2179, 2021.

[27] M. Akbari and P. Asadi, "Effects of different cooling conditions on friction stir processing of A356 alloy: numerical modeling and experiment," *Proceedings of the Institution of Mechanical Engineers - Part C: Journal of Mechanical Engineering Science*, vol. 236, no. 8, pp. 4133–4146, 2022.

[28] M. Akbari and P. Asadi, "Dissimilar friction stir lap welding of aluminum to brass: modeling of material mixing using coupled Eulerian–Lagrangian method with experimental verifications," *Proceedings of the Institution of Mechanical Engineers - Part L: Journal of Materials: Design and Applications*, vol. 234, no. 8, pp. 1117–1128, 2020.

[29] T. F. Flint, J. A. Francis, M. C. Smith, and J. Balakrishnan, "Extension of the double-ellipsoidal heat source model to narrow-groove and keyhole weld configurations," *Journal of Materials Processing Technology*, vol. 246, pp. 123–135, 2017.

[30] R. M. Farias, P. R. F. Teixeira, and L. O. Vilarinho, "An efficient computational approach for heat source optimization in numerical simulations of arc welding processes," *Journal of Constructional Steel Research*, vol. 176, Article ID 106382, 2021.

[31] N. Nguyen and J. H. Chujutalli, "Simulating convective-radiative heat sink effect by means of FEA-based Gaussian heat sources and its approximate analytical solutions for semi-infinite body," *International Journal of Advanced Manufacturing Technology*, vol. 117, no. 11-12, pp. 3717–3742, 2021.

[32] V. García-García, J. C. Camacho-Arriaga, and F. Reyes-Calderón, "A simplified elliptic paraboloid heat source model for autogenous GTAW process," *International Journal of Heat and Mass Transfer*, vol. 100, pp. 536–549, 2016.

[33] H. Kitano and Y. Mikami, "Constructing a heat source parameter estimation model for heat conduction finite element analysis using deep convolutional neural network," *Materials Today Communications*, vol. 31, Article ID 103387, 2022.

[34] Y. Zhang, G. Chen, B. Chen, J. Wang, and C. Zhou, "Experimental study of hot cracking at circular welding joints of 42CrMo steel," *Optics & Laser Technology*, vol. 97, pp. 327–334, 2017.

[35] J. Park, G. An, N. Ma, and S. Kim, "Effect of transverse restraint on welding residual stress in V-groove butt welding," *Metals*, vol. 12, no. 4, p. 654, 2022.

[36] A. Tabatabaeian, A. R. Ghasemi, M. M. Shokrieh, B. Marzbanrad, M. Baraheni, and M. Fotouhi, "Residual stress in engineering materials: a review," *Advanced Engineering Materials*, vol. 24, no. 3, Article ID 2100786, 2022.

[37] Z. Liu, X. Hu, Z. Yang et al., "Optimization study of post-weld heat treatment for 12Cr1MoV pipe welded joint," *Metals*, vol. 11, no. 1, p. 127, 2021.

[38] X. Zhang, X. Zhang, M. Zhang, L. Sun, and M. Li, "Optimization design and flexible detection method of wall-climbing robot system with multiple sensors integration for magnetic particle testing," *Sensors*, vol. 20, no. 16, p. 4582, 2020.

[39] N. Amiri, G. H. Farrahi, K. R. Kashyzadeh, and M. Chizari, "Applications of ultrasonic testing and machine learning methods to predict the static & fatigue behavior of spot-welded joints," *Journal of Manufacturing Processes*, vol. 52, pp. 26–34, 2020.

[40] Q. Gao, X. Zhan, H. Shen, W. Ling, and H. Bu, "Effect of welding sequence on stress and deformation field of Invar alloy multi-layer and multi-pass welding: a simulation study," *Modern Physics Letters B*, vol. 34, no. 13, Article ID 2050129, 2020.

[41] F. Peng, Z. Feng, Y. Zhao, and J. Long, "A novel reticular retained austenite on the weld fusion line of low carbon martensitic stainless steel 06Cr13Ni4Mo and the influence on the mechanical properties," *Metals*, vol. 12, no. 3, p. 432, 2022.